Supplementary Information

Identifying superionic conductors by materials informatics and high-throughput synthesis

Supplementary Note 1. Training data and employed descriptors for machine-learning model

We compiled reliable 29 oxide-ion conductivities at 973K from literatures as training data, which listed in Supplementary Table 1[1-11]. In case of different oxide-ion conductivities among literatures, their averaged value was used.

We devised 92 handcrafted descriptors based on crystal structure and atomic properties. As described in main text, we then reduced the number of descriptors by the PLS-VIP algorithm to prevent from overfitting[12]. As the result, 26 important descriptors were remained as shown in Supplementary Table 2. These descriptors are classified into 5 types: (a) descriptors based on radial distribution function, (b) descriptors based on cation-centered polyhedrons[13], (c) descriptors based on bond valence sum[14, 15], (d) descriptors based on porosity as implemented in Zeo++[16, 17], and (e) atom-based descriptors.

Supplementary Table 1. Training data of oxide-ion conductivity at 973K.

No	Materials	(references)	Oxide-ion conductivity (Scm^{-1})
1	$Zr_{0.82}Y_{0.18}O_{1.82}$	(1,2)	1.19×10^{-2}
2	$Zr_{0.87}Ca_{0.13}O_{1.87}$	(1,2)	2.76×10^{-3}
3	$Th_{0.87}Y_{0.13}O_{1.87}$	(2)	1.42×10^{-3}
4	$Ce_{0.8}Gd_{0.2}O_{1.9}$	(2-5)	3.68×10^{-2}
5	$Ce_{0.8}Sm_{0.2}O_{1.9}$	(2-4)	3.41×10^{-2}
6	$Hf_{0.88}Ca_{0.12}O_{1.88}$	(2)	1.23×10^{-4}
7	Bi_2O_3	(6)	1.95×10^{-3}
8	$Bi_{1.5}Y_{0.5}O_3$	(2,6-8)	1.66×10^{-1}
9	$Bi_{1.71}W_{0.29}O_{3.435}$	(2)	4.75×10^{-2}
10	$BaZrO_3$	(8)	1.00×10^{-6}
11	$Ba_2Zr_2O_6$	(8)	1.00×10^{-6}
12	$Gd_2Ti_2O_7$	(3,4)	1.20×10^{-5}
13	$Ba_2In_2O_5$	(3,4,6,9)	2.78×10^{-4}
14	$Gd_2Zr_2O_7$	(3,4)	6.35×10^{-3}
15	$Gd_2Sn_2O_7$	(3,4)	9.48×10^{-7}
16	$Y_2Ti_2O_7$	(3,4)	2.06×10^{-2}
17	$NdAlO_3$	(6)	1.00×10^{-5}
18	Sr_2ScAlO_5	(6)	1.00×10^{-5}
19	$SrZrO_3$	(6) T = 1023 K	4.30×10^{-6}
20	$Ca_2Cr_2O_5$	(6)	5.00×10^{-3}
21	$Ba_4Zr_2In_2O_{11}$	(6)	1.00×10^{-2}
22	$Ba_8Zr_3In_5O_{24}$	(3,4,6)	2.59×10^{-3}
23	$Y_2Zr_2O_7$	(3,4)	3.16×10^{-4}
24	$La_4WMo_3O_{18}$	(4)	8.01×10^{-3}
25	$La_3BiMo_4O_{18}$	(3,10,11)	3.83×10^{-2}
26	$Sr_8Sc_5Al_3O_{20}$	(8)	1.00×10^{-3}
27	$La_4VMo_3O_{18}$	(11)	6.70×10^{-2}
28	$Ba_8Sc_5Zr_3O_{23}$	(6)	7.00×10^{-3}
29	$V_7CuBi_{16}O_{42}$	(3,4)	1.31×10^{-1}

Supplementary Table 2. Extracted handcrafted descriptors by PLD-VIP method.

classification	No.	explain of descriptors
(a) Descriptors based on radial distribution function	1	Intercept in distance axis of the coordination number between oxygen atoms fitted by quadratic function
	2	Variance in distance axis direction from the coordination number between oxygen atoms fitted by quadratic function
	3	Base 10 logarithmic intercept in distance axis of the coordination number between cations fitted by quadratic function
	4	Variance in distance axis direction from the coordination number between cations fitted by quadratic function
	5	Base 10 logarithmic variance in coordination number between cations fitted by quadratic function
(b) Descriptors based on cation-centered polyhedrons	6	Distortion index in VESTA[13]
	7	Bond angle variance in VESTA[13]
	8	Effective coordination number of the cation-centered polyhedrons in VESTA[13]
(c) Descriptors based on bond valence sum	9	Base 10 logarithmic deviation of BVS from 2 along the percolation path (BVS channel)
	10	Minimum deviation BVS from 2 at oxygen position in the crystal
	11	Minimum volume fraction of BVS channel to the unit cell volume
	12	Minimum tortuosity of BVS channel
	13	Minimum value of averaged diameter for BVS channel along the path
	14	Base 10 logarithmic minimum value for the cross section/tortuosity ratio of BVS channel
	15	Base 10 logarithmic maximum value for the cross section/sinuosity ratio of BVS channel
	16	Minimum value of the cross section/path length ratio of BVS potential (V_{BVS}) along the path
	17	Minimum volume fraction of V_{BVS} to the unit cell volume along the path
	18	Base 10 logarithmic minimum tortuosity of V_{BVS} along the path
	19	Minimum value for average diameter of V_{BVS} along the path
(d) Descriptors based on porosity	20	Largest free sphere diameter percolating the crystal except oxygens
	21	Volume fraction of void channel to the unit cell volume except oxygens
(e) Atom-based descriptors	22	The number density of atoms
	23	The number density of oxygen atoms
	24	Base 10 logarithmic number density of cations
	25	Base 10 logarithmic average electronegativity of atoms in the unit cell except oxygens
	26	Base 10 logarithmic melting point predicted from constituent binary oxides by Neumann Kopp's law

Supplementary Note 2. Supplementary information about elemental selections

If we select other good structure as the reference for the SOAP distance, we could find other elements to be recommended for the following combinatorial experiments. To illustrate this, we also selected $Bi_{1.5}Y_{0.5}O_3$ (case 2), $La_3BiMo_4O_{18}$ (case 3), and $Ce_{0.8}Sm_{0.2}O_{1.9}$ or $Ce_{0.8}Gd_{0.2}O_{1.9}$ (case 4) as reference materials for local structure similarity criterion, and examined which elements were included in the high conductivity materials ($\sigma > 10^{-3}$ Scm^{-1}). The results are illustrated in Supplementary Figures 1b-d. After eliminating toxic elements, noble metals, and 3d-transition metals, as similar to the case 1 described in the main text, we list the elements of candidates as shown in Supplementary Table 3. It can be seen that as the reference material differs, the selected elements also vary. This is a consequence that good conductivity can result from not a unique structure but some different local structures. In other words, taking a different reference, we have another chance to discover good materials.

We also investigated the frequencies of elements found in the materials under following criteria; the SOAP distance for $V_7CuBi_{16}O_{42}$ is less than 0.6 ($d < 0.6$) and the predicted conductivity at 973K is *less than* 10^{-3} Scm^{-1} ($\sigma < 10^{-3}$ Scm^{-1}). The results are shown in the case 5 in Supplementary Table 3 and Supplementary Figure 1e. The materials with lower conductivity include distinguishably Mg and Al instead of Nb and alkaline earth metals as in the case 1. Therefore, the discovery of m-BC phase (e.g., $Bi_{0.74}Ca_{0.26}O_{1.37}$) and its stabilization with Nb and Ta could not be achieved if we took the case 5. Finally, we examined the frequencies of elements for the materials $\sigma < 10^{-3}$ Scm^{-1} without any restriction of the SOAP distance as shown in the case 6 in Supplementary Table 3 and Supplementary Figure 1f. A large frequency of Si appears in this case and suggests the local structure with respect to Si is not recommended by our approach.

Supplementary Table 3. Elements selected by using different reference material for the SOAP distance and/or different conductivity criterion.

Case	Reference materials	Predicted σ (Scm^{-1})	Selected elements
(1)	$V_7CuBi_{16}O_{42}$	$> 10^{-3}$	Bi, Nb, Ta, Sr/Ca/Ba
(2)	$Bi_{1.5}Y_{0.5}O_3$	$> 10^{-3}$	Nb, Bi, Mo, Y
(3)	$La_3BiMo_4O_{18}$	$> 10^{-3}$	Al, Ge, W, Si
(4)	$Ce_{0.8}Sm_{0.2}O_{1.9}$ / $Ce_{0.8}Gd_{0.2}O_{1.9}$	$> 10^{-3}$	Ce, Zr, Pr, Tb
(5)	$V_7CuBi_{16}O_{42}$	$< 10^{-3}$	Bi, Ta, Mg, Al
(6)	-	$< 10^{-3}$	Si, Zr, Bi, Mo

The case 1 is studied in the high throughput experiment as described in the main text. Note that since the SOAP distance between $Ce_{0.8}Sm_{0.2}O_{1.9}$ and $Ce_{0.8}Gd_{0.2}O_{1.9}$ is very small (0.02), we selected both materials as reference.

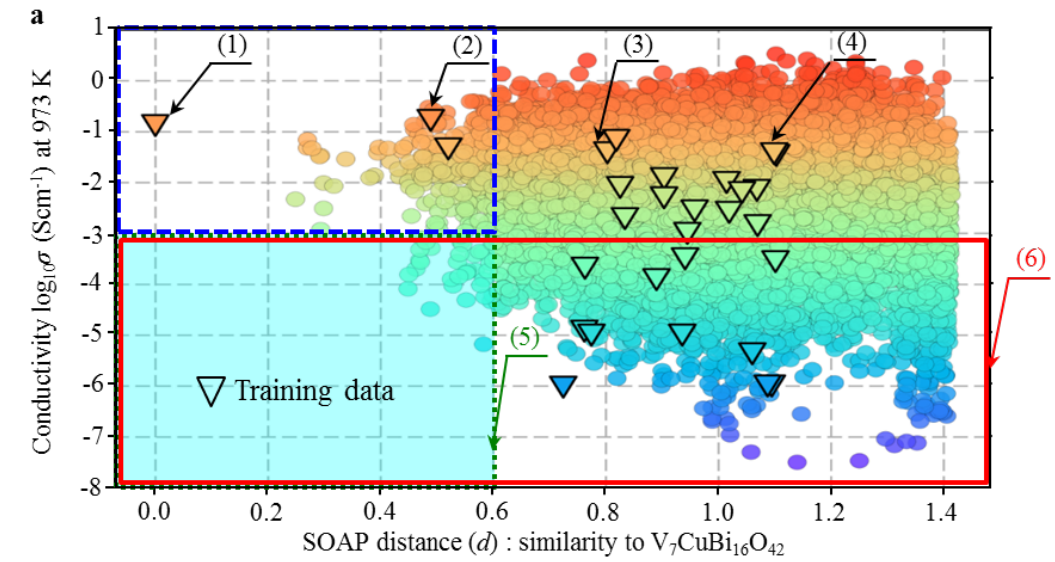
a
(1)
(2)
(3)
(4)
(5)
(6)
Training data
Conductivity $\log_{10}\sigma$ (Scm^{-1}) at 973 K
SOAP distance (d) : similarity to $V_7CuBi_{16}O_{42}$

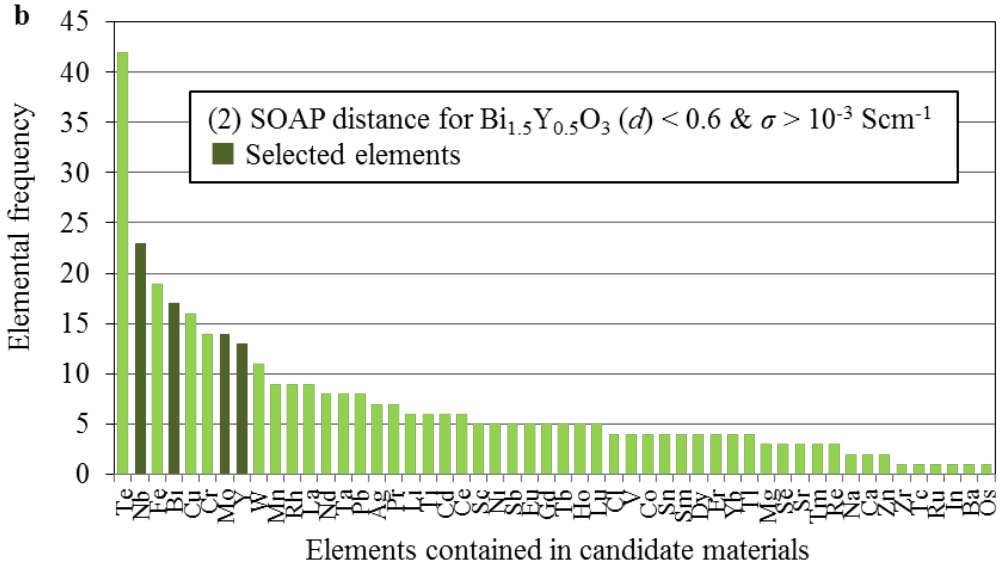
b
(2) SOAP distance for $Bi_{1.5}Y_{0.5}O_3$ (d) < 0.6 & σ > 10^{-3} Scm^{-1}
Selected elements
Elemental frequency
Elements contained in candidate materials

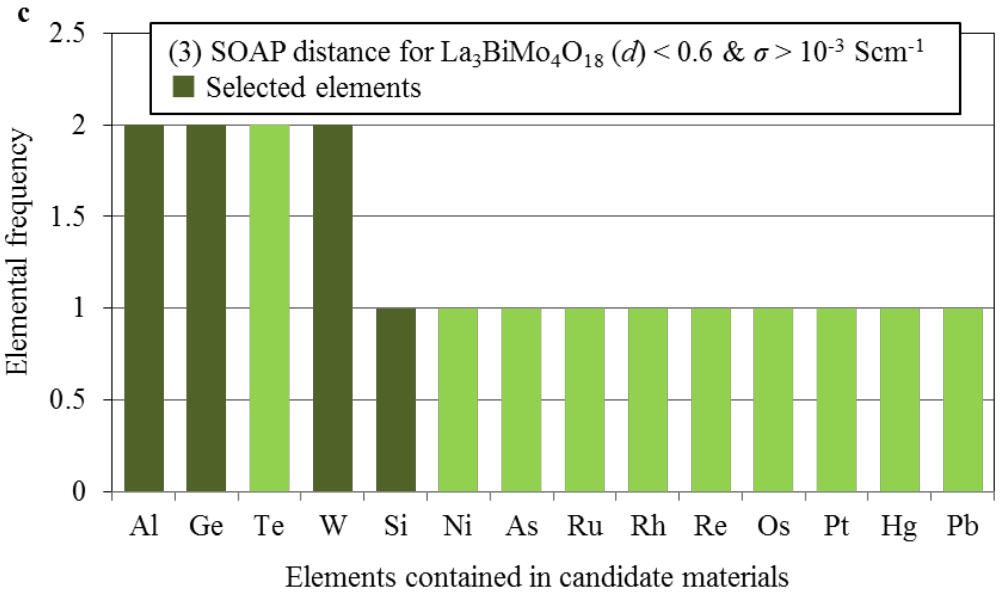
c
(3) SOAP distance for $La_3BiMo_4O_{18}$ (d) < 0.6 & σ > 10^{-3} Scm^{-1}
Selected elements
Elemental frequency
Al Ge Te W Si Ni As Ru Rh Re Os Pt Hg Pb
Elements contained in candidate materials

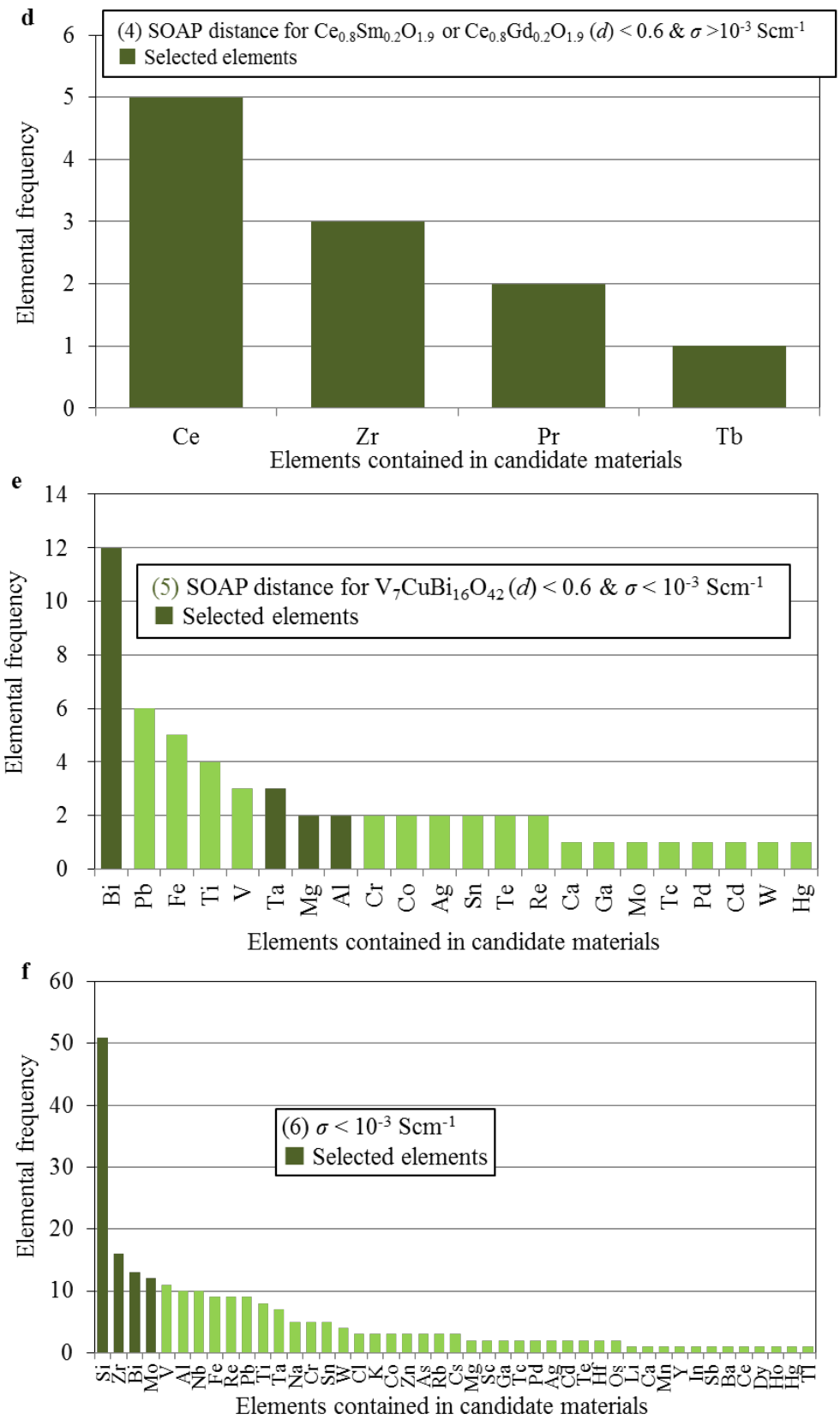

Supplementary Figure 1. Analyses of the frequencies of elements included in the materials which are selected using the criteria listed in Supplementary Table 3 and illustrated in the mapping **a**.

Supplementary Note 3. Characterization of library films

Supplementary Figure 2a displays a photograph of typical library films prepared on an alumina substrate. In some of the library films, phase separation and cracks were observed, but most of the samples were dense films without cracks. As an example, Supplementary Figures 2b and 2c show the microstructure of surface and cross-section of $Ca_{0.06}(Nb_{0.056}Ta_{0.084})Bi_{0.8}O_{1.61}$ (x = 0.3, y = 0.6, z = 0.8) thin film, respectively. This film exhibited dense microstructure with nano-sized grains about 100 nm and a thickness of about 1 μm.

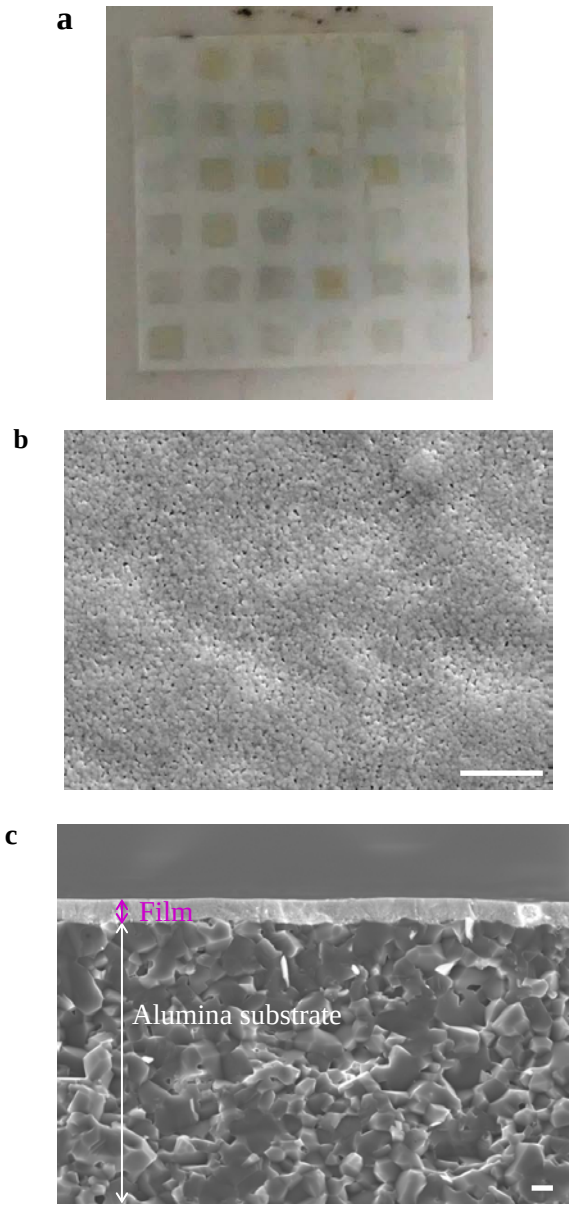

Supplementary Figure 2. a Photograph of library films deposited on the alumina substrate. **b** Secondary electron microscope images of surface microstructure. **c** Cross-section microstructure for $Ca_{0.06}(Nb_{0.056}Ta_{0.084})Bi_{0.8}O_{1.61}$ library film as typical sample. The Scale bars for **b** and **c** represent 1 μm.

In order to confirm the existing phases in library films, we measured high-throughput XRD with SPring-8 synchrotron radiation. Supplementary Figure 3 shows typical XRD patterns where the peak positions in these figures are converted into those for CuKα X-ray wavelength to compare with the JCPDS peak positions. As a low temperature phase of Bi_2O_3, monoclinic structure (α-phase) is known, but various dopants, such as Ta_2O_5 or Nb_2O_5 stabilize defect fluorite structure (δ-phase)[18] which is usually stable at higher temperature than 1003K[19]. In this study, the peak position of library films with Bi content $z \geq 0.6$ for many compositions coincided with that of defect fluorite or fluorite-related structures so called δ-phase despite the kind of dopants, as typically shown in Supplementary Figure 3a. Supplementary Figure 3b shows diffraction peaks for the all samples with $z = 0.5$ where the each sample number corresponds to those in Supplementary Figure 3c. Among these compositions, the main diffraction peaks position of samples with $z = 0.5$ and $x = 0.8$ matched with those of CaO-doped bismuth oxides such as $Bi_8Ca_3O_{15}$[20] or $Bi_{20}Ca_7NbO_{39.5}$[21]. The crystal structure of $Bi_{20}Ca_7NbO_{39.5}$ has been reported to be disordered δ-Bi_2O_3-related monoclinic superstructure (hereafter referred to m-BC) which differs from the structure of monoclinic α-Bi_2O_3[20]. Highly disordered oxygen sublattice in such crystal structure is advantageous for high ionic conductivity[22].

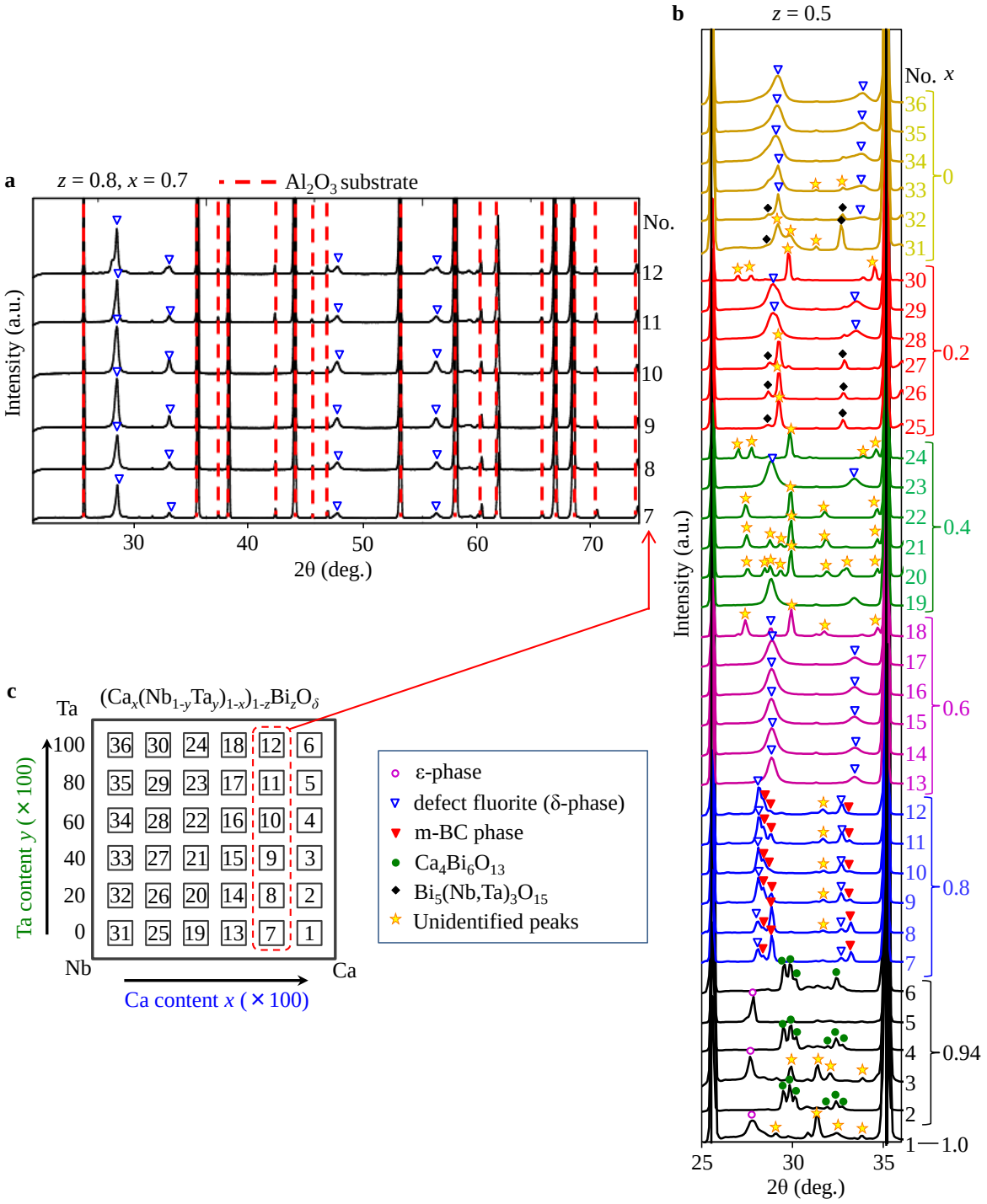

Supplementary Figure 3. Typical X-ray diffraction (XRD) profiles of [$(Ca_x(Nb_{1-y}Ta_y)_{1-x})_{1-z}Bi_zO_\delta$; $\delta = ((5-3x)\times(1-z)+3z)/2$] library films: **a** $z = 0.8$ and $x = 0.7$, **b** $z = 0.5$; **c** Relationship between library number and each film position on an alumina substrate. The numbers on the right side in **a** and **b** indicate library number. Ca content (x) corresponding to the each library number for $z = 0.5$ is also shown in **b**. The 2θ values indicated in these figures correspond to those of CuKα wavelength.

Supplementary Figures 4 and 5 display the conductivity mapping of $(AE_x(Nb_{1-y}Ta_y)_{1-x})_{1-z}Bi_zO_\delta$ [AE = Ca, Sr, Ba] library films at 873K and 973K, respectively. To see the chemical trend, conductivities at 973K for the compositional parameters *x*, *y* and *z* are summarized in Supplementary Table 4. The structural classification by SOAP metric indicated that the alkaline earth (AE) elements, namely Ca, Sr and Ba would contribute local structural similarity to $V_7CuBi_{16}O_{42}$. In order to confirm the effect of kind of AE elements on the conductivity, we firstly fabricated library films containing AE elements ($z = 0.8$ and $x \geq 0.7$). The samples containing any of the AE elements showed high conductivity. Particularly, Ca and Ba were revealed to be effective for the high conductivity as shown in Supplementary Figure 4i. However, the melting point of Ba containing films was so low that they could be unstable thermally. Therefore, Ca was selected as typical AE element. The increase of Bi content *z* enhanced the conductivity, and the maximum conductivity of 2.2×10^{-1} Scm^{-1} at 973K was achieved for defect fluorite-structured sample of $z = 0.8$ (with $x = 0.7$ and $y = 0.2$). Furthermore, the conductivity for series of library films tended to be maximized at $x = 0.7$ to 0.8 for any *z* and *y* values in many cases, which contained m-BC phase mainly. Defect fluorite-structured bismuth oxide is known to exhibit high oxide-ion conductivity due to its highly disordered structure[22], although its thermal stability is low[23]. By contrast, it was found that the library films containing m-BC phase had both high conductivity and thermal stability as explained in main manuscript.

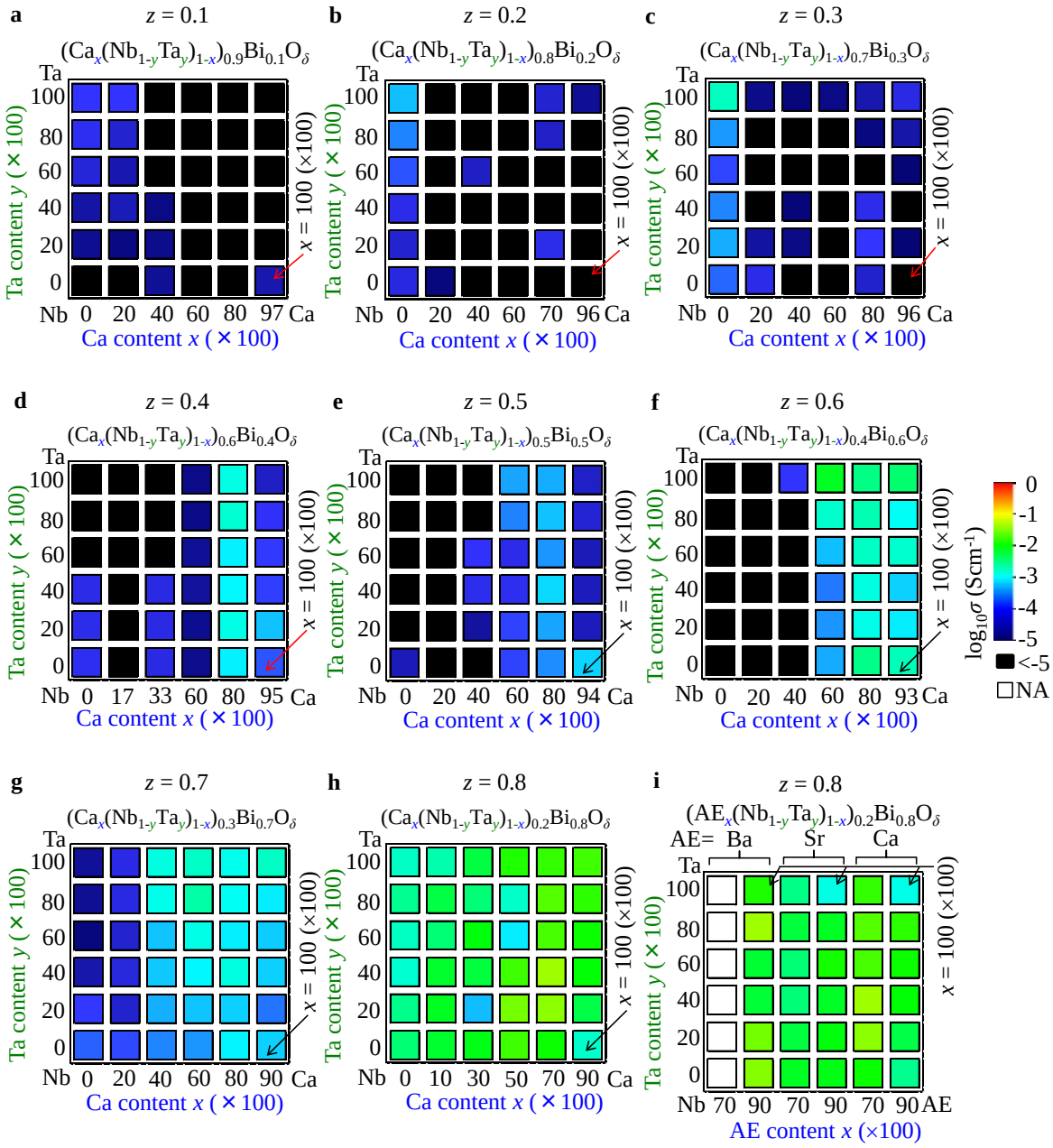

Supplementary Figure 4. Conductivity mapping of [(Ca$_x$(Nb$_{1-y}$Ta$_y$)$_{1-x}$)$_{1-z}$Bi$_z$O$_\delta$; δ = ((5-3x)×(1-z)+3z)/2] library films measured at 873 K: **a** z = 0.1, **b** z = 0.2, **c** z = 0.3, **d** z = 0.4, **e** z = 0.5, **f** z = 0.6, **g** z = 0.7, **h** z = 0.8, and **i** conductivity mapping of [(AE$_x$(Nb$_{1-y}$Ta$_y$)$_{1-x}$)$_{0.2}$Bi$_{0.8}$O$_\delta$; x = 0.7 or 0.9; AE = Ca or Sr or Ba] library films measured at 873 K. The conductivity for a part of Ba containing samples could not be evaluated because they melted during the conductivity measurement at 873K.

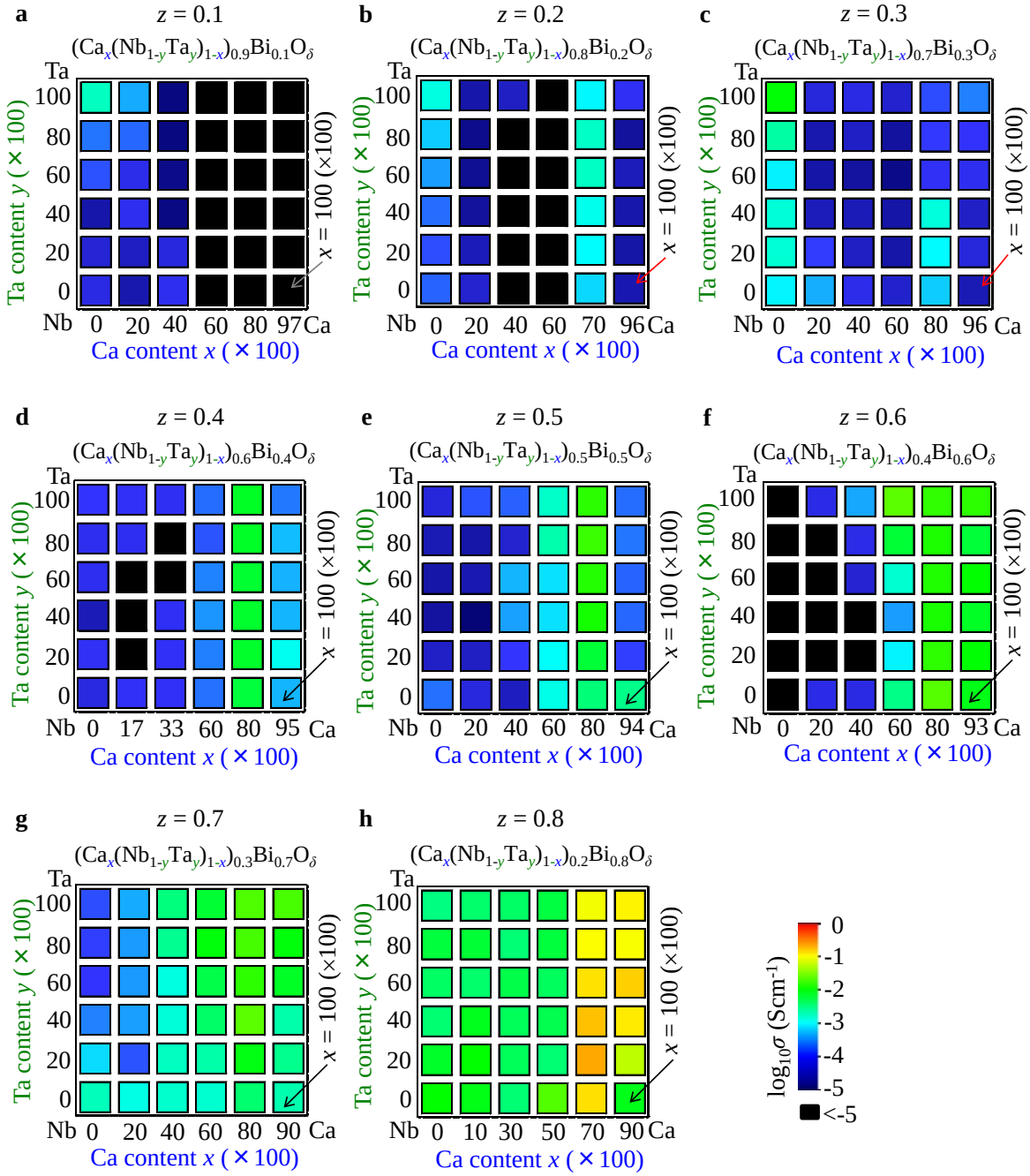

Supplementary Figure 5. Conductivity mapping of [(Ca$_x$(Nb$_{1-y}$Ta$_y$)$_{1-x}$)$_{1-z}$Bi$_z$O$_\delta$; δ = ((5-3x)×(1-z)+3z)/2] library films measured at 973 K: **a** z = 0.1, **b** z = 0.2, **c** z = 0.3, **d** z = 0.4, **e** z = 0.5, **f** z = 0.6, **g** z = 0.7, and **h** z = 0.8.

Supplementary Table 4. The conductivity for the library films measured at 973K.

No.	*z*	*x*	*y*	Conductivity (Scm^{-1})	*z*	*x*	*y*	Conductivity (Scm^{-1})	*z*	*x*	*y*	Conductivity (Scm^{-1})
1	0.1	1.0	0	-	0.2	1.0	0	3.1×10^{-5}	0.3	1.0	0	3.3×10^{-5}
2		0.97	0.2	-		0.96	0.2	2.6×10^{-5}		0.96	0.2	5.9×10^{-5}
3			0.4	-			0.4	2.9×10^{-5}			0.4	4.3×10^{-5}
4			0.6	-			0.6	3.6×10^{-5}			0.6	8.1×10^{-5}
5			0.8	-			0.8	2.3×10^{-5}			0.8	9.6×10^{-5}
6			1.0	-			1.0	8.7×10^{-5}			1.0	2.4×10^{-4}
7		0.8	0	-		0.7	0	6.4×10^{-4}		0.8	0	5.7×10^{-4}
8			0.2	-			0.2	9.9×10^{-4}			0.2	9.8×10^{-4}
9			0.4	-			0.4	1.2×10^{-3} *			0.4	1.4×10^{-3}
10			0.6	-			0.6	1.7×10^{-3}			0.6	8.9×10^{-5}
11			0.8	-			0.8	1.7×10^{-3}			0.8	1.1×10^{-4}
12			1.0	-			1.0	9.3×10^{-4}			1.0	1.3×10^{-4}
13		0.6	0	-		0.6	0	-		0.6	0	4.8×10^{-5}
14			0.2	-			0.2	-			0.2	2.7×10^{-5}
15			0.4	-			0.4	-			0.4	2.7×10^{-5}
16			0.6	-			0.6	-			0.6	1.7×10^{-5}
17			0.8	-			0.8	-			0.8	2.3×10^{-5}
18			1.0	-			1.0	-			1.0	4.8×10^{-5}
19		0.4	0	8.1×10^{-5}		0.4	0	-		0.4	0	7.3×10^{-5}
20			0.2	6.2×10^{-5}			0.2	-			0.2	4.1×10^{-5}
21			0.4	1.6×10^{-5}			0.4	-			0.4	3.4×10^{-5}
22			0.6	1.8×10^{-5}			0.6	-			0.6	2.4×10^{-5}
23			0.8	1.5×10^{-5}			0.8	-			0.8	4.2×10^{-5}
24			1.0	1.5×10^{-5}			1.0	4.2×10^{-5}			1.0	6.8×10^{-5}
25		0.2	0	3.0×10^{-5}		0.2	0	4.9×10^{-5}		0.2	0	$4.0\times´10^{-4}$
26			0.2	4.0×10^{-5}			0.2	3.5×10^{-5}			0.2	1.1×10^{-4}
27			0.4	8.1×10^{-5}			0.4	2.3×10^{-5}			0.4	3.6×10^{-5}
28			0.6	7.5×10^{-5}			0.6	2.0×10^{-5}			0.6	2.7×10^{-5}
29			0.8	1.8×10^{-4}			0.8	1.8×10^{-5}			0.8	3.0×10^{-5}
30			1.0	3.9×10^{-4}			1.0	2.8×10^{-5}			1.0	5.8×10^{-5}
31		0	0	6.8×10^{-5}		0	0	1.7×10^{-4}		0	0	9.0×10^{-4}
32			0.2	5.4×10^{-5}			0.2	1.4×10^{-4}			0.2	1.5×10^{-3}
33			0.4	2.8×10^{-5}			0.4	1.9×10^{-4}			0.4	1.4×10^{-3}
34			0.6	1.4×10^{-4}			0.6	3.4×10^{-4}			0.6	8.6×10^{-4}
35			0.8	2.1×10^{-4}			0.8	5.7×10^{-4}			0.8	2.3×10^{-3}
36			1.0	1.8×10^{-3}			1.0	1.3×10^{-3}			1.0	9.7×10^{-3}

No.	z	x	y	Conductivity (Scm^{-1})	z	x	y	Conductivity (Scm^{-1})	z	x	y	Conductivity (Scm^{-1})
1	0.4	1.0	0	4.4×10^{-4}	0.5	1.0	0	2.9×10^{-3}	0.6	1.0	0	8.1×10^{-3}
2		0.95	0.2	1.1×10^{-3}		0.94	0.2	1.2×10^{-4}		0.93	0.2	9.7×10^{-3}
3			0.4	4.4×10^{-4}			0.4	1.8×10^{-4}			0.4	7.2×10^{-3}
4			0.6	4.2×10^{-4}			0.6	1.7×10^{-4}			0.6	1.0×10^{-2}
5			0.8	4.7×10^{-4}			0.8	2.1×10^{-4}			0.8	6.0×10^{-3}
6			1.0	2.2×10^{-4}			1.0	1.9×10^{-4}			1.0	1.5×10^{-2}
7		0.8	0	5.8×10^{-3}		0.8	0	3.4×10^{-3}		0.8	0	2.2×10^{-2}
8			0.2	6.8×10^{-3}			0.2	6.1×10^{-3}			0.2	1.5×10^{-2}
9			0.4	6.7×10^{-3} *			0.4	1.2×10^{-2} *			0.4	1.2×10^{-2} *
10			0.6	6.4×10^{-3}			0.6	1.4×10^{-2}			0.6	1.3×10^{-2}
11			0.8	7.1×10^{-3}			0.8	1.7×10^{-2}			0.8	1.3×10^{-2}
12			1.0	7.3×10^{-3}			1.0	1.5×10^{-2}			1.0	1.5×10^{-2}
13		0.6	0	2.1×10^{-4}		0.6	0	1.2×10^{-3}		0.6	0	3.0×10^{-3}
14			0.2	2.4×10^{-4}			0.2	1.0×10^{-3}			0.2	8.8×10^{-4}
15			0.4	3.0×10^{-4}			0.4	7.2×10^{-4}			0.4	3.3×10^{-4}
16			0.6	2.5×10^{-4}			0.6	7.2×10^{-4}			0.6	1.5×10^{-3}
17			0.8	1.5×10^{-4}			0.8	2.1×10^{-3}			0.8	6.2×10^{-3}
18			1.0	1.9×10^{-4}			1.0	1.6×10^{-3}			1.0	2.3×10^{-2}
19		0.33	0	9.0×10^{-5}		0.4	0	3.9×10^{-5}		0.4	0	6.8×10^{-5}
20			0.2	9.0×10^{-5}			0.2	1.0×10^{-4}			0.2	-
21			0.4	8.6×10^{-5}			0.4	3.5×10^{-4}			0.4	-
22			0.6	-			0.6	4.4×10^{-4}			0.6	5.2×10^{-5}
23			0.8	-			0.8	4.9×10^{-5}			0.8	7.1×10^{-5}
24			1.0	8.5×10^{-5}			1.0	1.7×10^{-4}			1.0	3.7×10^{-4}
25		0.17	0	9.1×10^{-5}		0.2	0	6.1×10^{-5}		0.2	0	7.1×10^{-5}
26			0.2	-			0.2	4.1×10^{-5}			0.2	-
27			0.4	-			0.4	1.3×10^{-5}			0.4	-
28			0.6	-			0.6	3.1×10^{-5}			0.6	-
29			0.8	8.3×10^{-5}			0.8	2.7×10^{-5}			0.8	-
30			1.0	9.1×10^{-5}			1.0	1.4×10^{-4}			1.0	7.0×10^{-5}
31		0	0	6.4×10^{-5}		0	0	2.0×10^{-4}		0	0	-
32			0.2	8.9×10^{-5}			0.2	4.3×10^{-5}			0.2	-
33			0.4	3.4×10^{-5}			0.4	2.4×10^{-5}			0.4	-
34			0.6	8.0×10^{-5}			0.6	2.7×10^{-5}			0.6	-
35			0.8	8.0×10^{-5}			0.8	3.3×10^{-5}			0.8	-
36			1.0	$1.0\times´10^{-4}$			1.0	5.7×10^{-5}			1.0	-

No.	z	x	y	Conductivity (Scm^{-1})	z	x	y	Conductivity (Scm^{-1})
1	0.7	1.0	0	2.1×10^{-3}	0.8	1.0	0	8.0×10^{-3}
2		0.9	0.2	2.8×10^{-3}		0.9	0.2	5.6×10^{-2}
3			0.4	2.2×10^{-3}			0.4	1.2×10^{-1}
4			0.6	7.2×10^{-3}			0.6	1.5×10^{-1}
5			0.8	9.2×10^{-3}			0.8	9.6×10^{-2}
6			1.0	1.9×10^{-2}			1.0	1.1×10^{-1}
7		0.8	0	3.7×10^{-3}		0.7	0	1.3×10^{-1}
8			0.2	8.5×10^{-3}			0.2	2.2×10^{-1}
9			0.4	2.3×10^{-2} *			0.4	1.8×10^{-1} *
10			0.6	1.5×10^{-2}			0.6	1.3×10^{-1}
11			0.8	1.9×10^{-2}			0.8	9.9×10^{-2}
12			1.0	2.0×10^{-2}			1.0	9.0×10^{-2}
13		0.6	0	1.5×10^{-3}		0.5	0	2.1×10^{-2}
14			0.2	2.2×10^{-3}			0.2	3.6×10^{-3}
15			0.4	3.9×10^{-3}			0.4	5.0×10^{-3}
16			0.6	5.2×10^{-3}			0.6	4.3×10^{-3}
17			0.8	9.1×10^{-3}			0.8	5.8×10^{-3}
18			1.0	6.4×10^{-3}			1.0	5.7×10^{-3}
19		0.4	0	1.6×10^{-3}		0.3	0	3.6×10^{-3}
20			0.2	1.8×10^{-3}			0.2	4.5×10^{-3}
21			0.4	1.4×10^{-3}			0.4	4.5×10^{-3}
22			0.6	1.3×10^{-3}			0.6	5.2×10^{-3}
23			0.8	2.7×10^{-3}			0.8	3.5×10^{-3}
24			1.0	3.3×10^{-3}			1.0	4.1×10^{-3}
25		0.2	0	1.3×10^{-3}		0.1	0	8.3×10^{-3}
26			0.2	1.4×10^{-4}			0.2	1.0×10^{-2}
27			0.4	3.4×10^{-4}			0.4	7.8×10^{-3}
28			0.6	3.2×10^{-4}			0.6	3.8×10^{-3}
29			0.8	3.2×10^{-4}			0.8	6.2×10^{-3}
30			1.0	4.0×10^{-4}			1.0	3.8×10^{-3}
31		0	0	1.9×10^{-3}		0	0	1.0×10^{-2}
32			0.2	6.8×10^{-4}			0.2	6.9×10^{-3}
33			0.4	2.5×10^{-4}			0.4	3.6×10^{-3}
34			0.6	1.0×10^{-4}			0.6	4.1×10^{-3}
35			0.8	1.2×10^{-4}			0.8	5.8×10^{-3}
36			1.0	1.4×10^{-4}			1.0	3.1×10^{-3}

The conductivities corresponding to those for the bulk samples in Supplementary Table 5 are marked by the asterisk (*) and underline.

Supplementary Note 4. Characterization of bulk samples

As a result of high-throughput conductivity measurement for $(Ca_x(Nb_{1-y}Ta_y)_{1-x})_{1-z}Bi_zO_\delta$ library films, their conductivity was found to be maximum at x = 0.7 to 0.8 in almost all cases as described above. However, it was difficult to clarify the exact coexisting phases and their crystal structures from library films data alone. Therefore, we prepared bulk samples by solid-state reaction method, which have typical composition with x = 0.7 to 0.8 and y = 0.4 corresponding to the library number 9 in Supplementary Figure 3c for each z value. Supplementary Figures 6a-6f show the XRD pattern of bulk samples with z = 0.2, 0.4, 0.5, 0.6, 0.7 and 0.8. In the Supplementary figures 6g-6i, the XRD patterns of $Bi_{0.74}Ca_{0.26}O_{1.37}$ are also included as an example of m-BC-structured compound. The main phase of the sample with z = 0.8 was identified as δ-phase, which is consistent with the experimental results for library films as shown in Supplementary Figure 3a. In the compositional range of $0.5 \leq z \leq 0.7$, almost all peak position matched with those of m-BC phase which typically appeared for CaO-doped bismuth oxide such as $Bi_8Ca_3O_{15}$ over 1046 K[20] as shown in Supplementary Figures 6b–6d. Both $Bi_{0.74}Ca_{0.26}O_{1.37}$ samples quenched at 1073 K and sintered at 1073 K were also identified to be m-BC phase as shown in Supplementary Figures 6g and 6h, respectively. Meanwhile, $Bi_{0.74}Ca_{0.26}O_{1.37}$ bulk sample exhibited phase transition from m-BC phase to triclinic phase during measurement of conductivity at 973 K (Supplementary Figure 6i). This is because m-BC phase is usually metastable below 1046 K. On the other hand, much secondary phases besides m-BC phase were observed at $0.4 \geq z$, as shown in Supplementary Figures 6e and 6f.

We also analyzed crystal structure of bulk samples with z = 0.5, 0.6 and 0.7 by Rietveld method based on the m-BC structure[21]. The peak pattern for samples with z = 0.5 and 0.6 matched well with that of m-BC phase. The peak position of sample with z = 0.7 also matched well with that of m-BC phase. By contrast, for sample with z = 0.7, the peak intensity at the position where peaks overlap with those of defect fluorite phase tended to be relatively high (Supplementary Figure 6b). It suggests that the sample with z = 0.7 could contain defect fluorite phase in addition to m-BC phase, although two kinds of peaks are difficult to be separated. The lattice parameters of the main phase in each bulk sample, which are estimated by Rietveld method, are listed in Supplementary Table 5 with conductivities evaluated at 973K. In the case of z =0.8, the defect fluorite structure is slightly distorted from the cubic structure (referred to as δ'-phase), which probably results from the disordered oxygen sublattice that may contribute to a high conductivity as previously reported[22]. On the other hand, the change of lattice parameters for m-BC phase was relatively small among the nominal compositions examined.

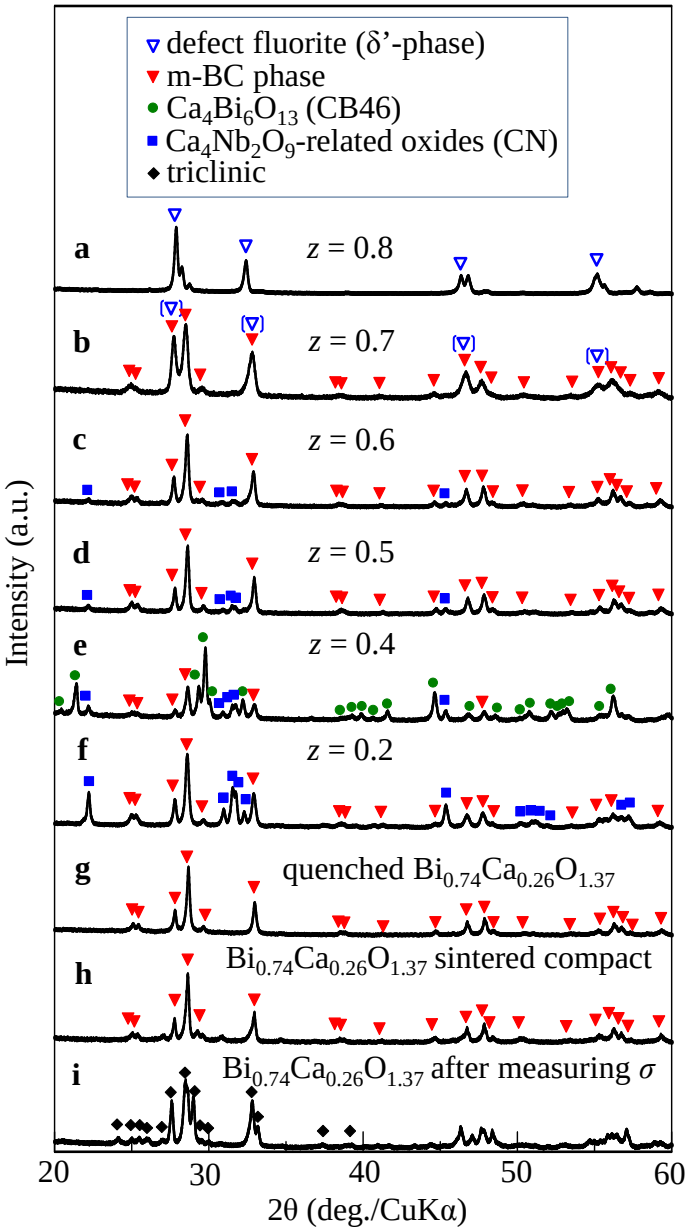

Supplementary Figure 6. X-ray diffraction (XRD) profiles of $[(Ca_x(Nb_{0.6}Ta_{0.4})_{1-x})_{1-z}Bi_zO_\delta$; δ = ((5-3x)×(1-z)+3z)/2] and $Bi_{0.74}Ca_{0.26}O_{1.37}$ bulk samples: **a** z = 0.8, **b** z = 0.7, **c** z =0.6, **d** z = 0.5, **e** z = 0.4, and **f** z = 0.2 for $(Ca_x(Nb_{0.6}Ta_{0.4})_{1-x})_{1-z}Bi_zO_\delta$. The compositions of these samples correspond to those of library number 9 in Supplementary Figure 3c. $Bi_{0.74}Ca_{0.26}O_{1.37}$ was quenched at 1073 K (**g**) and sintered at 1073 K for 2h (**h**). **i** XRD pattern of $Bi_{0.74}Ca_{0.26}O_{1.37}$ sintered compact after measuring conductivity at 973 K where diffraction peaks over 40° are not identified because the diffraction peak data for triclinic phase is reported only up to 40° in Powder Diffraction File (PDF#00-048-0215) database[19].

Supplementary Table 5. Summary of conductivity and XRD analysis for each bulk sample.

z	Nominal Composition	Conductivity (Scm^{-1}) at 973K	Main Phase	Secondary phases	Lattice Parameter of main phase					
					a (Å)	b (Å)	c (Å)	α (°)	β (°)	γ (°)
0.2	$Ca_{0.56}Nb_{0.144}Ta_{0.096}Bi_{0.2}O_{1.46}$	6.3×10^{-3}	m-BC	CN	9.34	3.79	9.61	90	110	90
0.4	$Ca_{0.48}Nb_{0.072}Ta_{0.048}Bi_{0.4}O_{1.38}$	1.5×10^{-3}	m-BC	CN+CB46	9.32	3.80	9.61	90	110	90
0.5	$Ca_{0.4}Nb_{0.06}Ta_{0.04}Bi_{0.5}O_{1.40}$	1.6×10^{-2}	m-BC	CN	9.33	3.79	9.59	90	110	90
0.6	$Ca_{0.32}Nb_{0.048}Ta_{0.032}Bi_{0.6}O_{1.42}$	2.8×10^{-2}	m-BC	CN	9.34	3.80	9.62	90	110	90
0.7	$Ca_{0.24}Nb_{0.036}Ta_{0.024}Bi_{0.7}O_{1.44}$	5.0×10^{-2}	m-BC	δ’-phase	9.37	3.79	9.60	90	110	90
0.8	$Ca_{0.14}Nb_{0.036}Ta_{0.024}Bi_{0.8}O_{1.49}$	1.5×10^{-1}	δ'-phase	-	5.50	5.50	5.51	91	90	89
0.74	$Ca_{0.26}Bi_{0.74}O_{1.37}$	8.6×10^{-3}	m-BC	-	9.33	3.80	9.61	90	110	90

CB46 and CN are abbreviations of $Ca_4Bi_6O_{13}$ and $Ca_4Nb_2O_9$-related oxides, respectively.

Supplementary Figure 7 shows temperature dependence of conductivity for bulk samples with z = 0.2, 0.4, 0.5, 0.6, 0.7, 0.8, $Bi_{0.74}Ca_{0.26}O_{1.37}$ and YSZ[24]. The sample with $z \geq$ 0.5 indicated superior conductivity to YSZ at 973 K. Particularly, the conductivity of sample with z = 0.8 reached as high as 1.5×10^{-1} Scm^{-1} at 973 K. This trend is consistent with the tendency for library films. The bulk sample with z = 0.7 which contains m-BC phase exhibited almost same conductivity as $Bi_{0.74}Ca_{0.26}O_{1.37}$ bulk sample below 973 K, but the conductivity of $Bi_{0.74}Ca_{0.26}O_{1.37}$ degraded rapidly during impedance measurement at 973 K for few minutes due to the phase transition. In contrast, the conductivity of bulk sample with z = 0.7 increased linearly up to 973 K without degradation.

The ratio of m-BC phase to the other secondary phases was estimated for the samples except z = 0.8 by using XRD peak intensity of Supplementary Figure 6 as follows.

$$\frac{I_m}{I_{\mathrm{m}}+I_{s1}+I_{s2}+\cdots}\times 100\ \ (\%) \qquad \text{(S1)}$$

where I_{m}, I_{s1} and I_{s2} represent highest peak intensity of m-BC phase, 1st secondary phase and 2nd secondary phase, respectively. The conductivity of bulk samples increased depending on the m-BC phase content, as shown in main manuscript (Fig. 4c). Note that Fig. 4c doesn’t include the data of z = 0.7 because the exact amount of m-BC phase cannot be determined due to the difficulty of peak separation.

The results from the both libraries and bulk samples lead a consistent conclusion that the high conductivity is attributed from the m-BC phase which is significantly stabilized by coexistence of Ca and Nb/Ta.

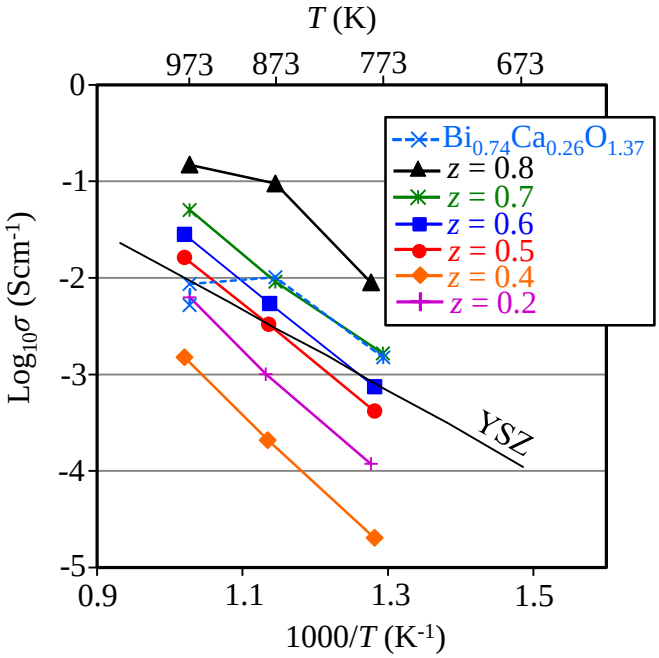

Supplementary Figure 7. Temperature dependence of conductivity (σ) for $[(Ca_x(Nb_{0.6}Ta_{0.4})_{1-x})_{1-z}Bi_zO_\delta$; $\delta = ((5-3x)\times(1-z)+3z)/2]$ and $Bi_{0.74}Ca_{0.26}O_{1.37}$ sintered compacts. In this figure, the conductivity of YSZ is also plotted from the literature[24].

Supplementary References:

1. Lacorre, P., Goutenoire, F., Bohnke, O., Retoux, R. & Laligant, Y. Designing fast oxide-ion conductors based on $La_2Mo_2O_9$. *Nature* **404**, 856–858 (2000).
2. Gellings, P. J., Bouwmeester, H. *Handbook of solid state electrochemistry* (CRC press, 1997).
3. Kharton, V. V., Marques, F. M., Kilner, J. A. & Atkinson, A. *Solid State Electrochemistry I: Fundamentals, Materials and their Applications Ch. 9* (Wiley-VCH, Weinheim, 2009).
4. Kharton, V. V., Marques, F. M. B., Atkinson, A. Transport properties of solid oxide electrolyte ceramics: a brief review. *Solid State Ionics* **174**, 135–149 (2004).
5. Steele, B. C. Appraisal of $Ce_{1-y}Gd_yO_{2-y/2}$ electrolytes for IT-SOFC operation at 500°C. *Solid state ionics* **129**, 95–110 (2000).
6. Kendall K. R. *et al*. Recent developments in perovskite-based oxide ion conductors. *Solid State Ionics* **82**, 215–223 (1995).
7. Brett, D. J., Atkinson, A., Brandon, N. P. & Skinner, S. J. Intermediate temperature solid oxide fuel cells. *Chem. Soc. Rev.* **37**, 1568–1578 (2008).

8. Boivin, J., Mairesse, G. Recent Material Developments in Fast Oxide Ion Conductors. *Chem. Mater*. **10**, 2870–2888 (1998).

9. Fop, S. *et al*. Oxide Ion Conductivity in the Hexagonal Perovskite Derivative $Ba_3MoNbO_{8.5}$. *J. Am. Chem. Soc.* **138**, 16764–16769 (2016).

10. Corbel, G., Selmi, A., Suard, E. & Lacorre, P. "Free" Volume Expansion and Formation Enthalpy of Defects as Key Parameters Tuning the Oxide Ionic Conductivity in Derivatives of β-$La_2Mo_2O_9$.*Chem. Mater.* **26**, 6838–6851 (2014).

11. Marozau, I. P. *et al*. Transport properties and thermal expansion of $La_2Mo_2O_9$-based solid electrolytes. *Mater. Res. Bull.* **40**, 361–371 (2005).

12. Chong, I. -G. & Jun, C. -H. Performance of some variable selection methods when multicollinearity is present. *Chemom. Intell. Lab. Syst.* **78**, 103–112 (2005).

13. Momma, K. & Izumi, F., VESTA 3 for three-dimensional visualization of crystal, volumetric and morphology data. *Journal of applied crystallography* **44**, 1272–1276 (2011).

14. Brown, I. D. Recent Developments in the Methods and Applications of the Bond Valence Model. *Chemical Reviews* **109**, 6858–6919 (2009).

15. Adams, S. & Rao, R. P. High power lithium ion battery materials by computational design. *Physica status solidi (a)* **208**, 1746–1753 (2011).

16. Willems, T. F., Rycroft, C. H., Kazi, M., Meza, J. C. & Haranczyk, M. Algorithms and tools for high-throughput geometry-based analysis of crystalline porous materials. *Micropor. Mesopor. Mat.* **149**, 134–141 (2012).

17. Ongari, D., Boyd, P. G., Barthel, S., Witman, M., Haranczyk, M. & Smit, B., Accurate characterization of the pore volume in microporous crystalline materials. *Langmuir* **33**, 14529–14538 (2017).

18. Sammes, N. M., Tompsett, G. A., Näfe, H. & Aldingera, F. Bismuth Based Oxide Electrolytes- Structure and Ionic Conductivity. *J. Euro Ceram. Soc.* **19**, 1801–1826 (1999).

19. Shuk, P., Wiemhöfer, H.-D., Guth, U., Göpel, W. & Greenblatt, M. Oxide ion conducting solid electrolytes based on B_2O_3. *Solid state Ionics* **89**, 179–196 (1996).

20. Burton, B. P. Rawn, C. J., Roth, R. S., Hwang, N. M. Phase equilibria and crystal chemistry in portions of the system SrO-CaO-Bi_2O_3-CuO, part IV–the system CaO-Bi_2O_3-CuO. *J. Res. Natl. Inst. Stand. Technol.* **98**, 469–516 (1993).

21. Thompson, M., Greaves, C. The structure and ionic conductivity of the fluorite-related isostructural materials $Bi_{20}Ca_7NbO_{39.5}$, $Bi_{10.75}Ca_{4.375}GaO_{22}$ and quenched Bi_9ReO_{17}. *Solid State Ionics* **181**, 1674–1679 (2010).
22. Yashima, M., Ishimura, D. Crystal structure and disorder of the fast oxide-ion conductor cubic Bi_2O_3. *Chem. Phys. Lett.* **378**, 395–399 (2003).
23. Shitara, K. *et al*. First-principles selection of solute elements for Er-stabilized Bi_2O_3 oxide-ion conductor with improved long-term stability at moderate temperatures. *Chem. Mater.* **29**, 3763–3768 (2017).
24. Malavasi, L., Fisher, C. A. & Islam, M. S. Oxide-ion and proton conducting electrolyte materials for clean energy applications: structural and mechanistic features. *Chem. Soc. Rev.* **39**, 4370–4387 (2010).